

Multimodal Augmented Reality Assisted Incision Guidance for Preoperative Tracheostomy Planning

Wenchao Yue[†], Yupeng Wang[†], Shuoyuan Chen, Huxin Gao, and Hongliang Ren*

Abstract—The tracheostomy procedure is crucial for situations involving intubation, airway blockages, or neck injuries, requiring precise incision placement to minimize risks and ensure effectiveness. Traditional methods involve palpating neck landmarks, but challenges arise in scenarios like teleoperation or critical care. Recent advancements in Augmented Reality (AR) and robotic-assisted surgery (RAS) offer promising solutions to enhance procedural safety and accuracy. In our study, we aim to explore the utilization of AR guidance in assisting tracheostomy incision localization. We employ a handheld ultrasound (US) probe to acquire preoperative anatomical data from a larynx phantom and convert ultrasound data into visual feedback, thus employing a multimodal approach that integrates US information into the visual domain. By marking the region of interest (ROI) on the laryngeal phantom model and importing it into the HoloLens 2 device, we achieve visual guidance for precise incision insertion within the ROI. Additionally, we conducted laser localization comparison experiments, comparing procedures performed with and without AR glasses. AR-guided incision localization exhibited impressive performance metrics with a high precision of 0.932 for the cricothyrotomy scene and 0.938 for standard tracheostomy while demonstrating minimal mean central positioning errors of 0.301 mm and 0.236 mm, respectively. The results demonstrate that AR guidance enables surgeons to locate the corresponding laryngeal area touchlessly, efficiently, and accurately, thereby facilitating the progress of robotic-assisted tracheostomy.

I. INTRODUCTION

Tracheostomy is a common procedure in intensive care units (ICUs) that can enhance the clinical management of critically ill patients by improving patient comfort, reducing sedation requirements, facilitating the weaning process, and expediting discharge from the ICU [1]–[3]. This procedure involves creating an artificial airway through a transverse incision between the tracheal cartilages, playing a crucial role in extending the duration of mechanical ventilation support [4]. Prior to tracheostomy surgery, surgeons typically employ palpation techniques on the tracheal surface to develop a tactile understanding of human anatomy [5]. They rely on force and deflection feedback obtained through palpation to identify a suitable incision site, often targeting

This work was supported in part by the Hong Kong Research Grants Council (RGC) Collaborative Research Fund (CRFC4026-21GF), RGC-General Research Fund (GRF) 14211420, and the Hong Kong Research Grants Council (RGC) Research Impact Fund (RIF-R4020-22), and in part by the Guangdong Basic and Applied Basic Research Foundation (GBABF) under Grant 2021B1515120035. (Corresponding Author: Hongliang Ren)

W. Yue, Y. Wang, S. Chen, H. Gao and H. Ren are with are with the Department of Electronic Engineering, The Chinese University of Hong Kong, Sha Tin, Hong Kong, China and CUHK Shenzhen Research Institute CUHK-SZRI, Shenzhen, China. wenchao.yue@link.cuhk.edu.hk; yupengwang@cuhk.edu.hk; hren@ieee.org;

[†]These two authors contributed equally to this work.

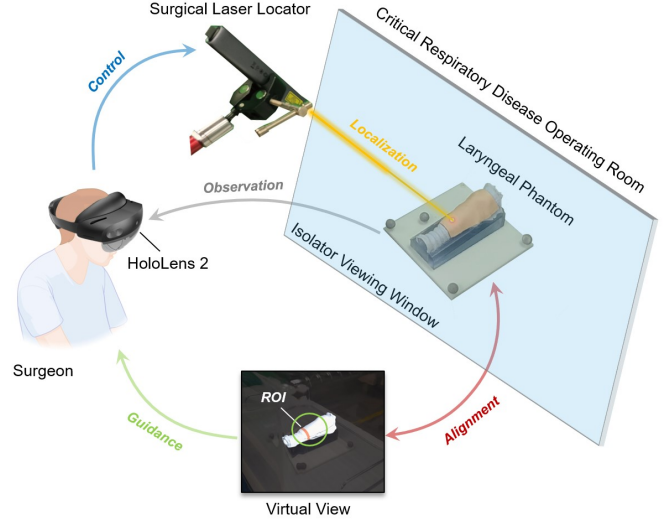


Fig. 1. The integration of AR technology, specifically HoloLens 2, and a Surgical Laser Locator in a tracheostomy procedure. The surgeon utilizes the AR capabilities to overlay virtual preoperative information onto the patient's anatomy, aiding in the precise localization of the incision site on the laryngeal regions. The Surgical Laser Locator further enhances accuracy by guiding the medical robots to the optimal position for the incision. This combination of AR technology and surgical tools enhances the precision and safety of tracheostomy procedures, ultimately improving patient outcomes.

the softer tracheal regions between the first and second tracheal cartilages or between the second and third cartilages [6], [7]. Therefore, precise identification of the tracheal rings and accurate localization of the incision site are essential considerations. Complications arising from errors in the initial tracheal incision can lead to serious outcomes such as pneumothorax, significant bleeding, or mortality [8], [9]. Consequently, meticulous placement of the incision and the tracheal window is crucial to prevent potential complications.

Robot-assisted minimally invasive surgery (RMIS) combines the advantages provided by surgical robots, such as tremor filtration, reduced muscle fatigue, 3D vision, and improved eye-hand coordination [10]–[13]. Several peer studies are currently exploring robot-assisted techniques in the tracheostomy process and optimizing the procedures to gain more possibilities for follow-up treatment success [14]–[18]. If the tactile feedback is visually relayed to the physician, it could expedite the tracheal intubation process and facilitate the prompt identification of the tracheal tube's placement. This, in turn, could provide additional time for life-saving resuscitation efforts [19].

AR stands out as a valuable tool for highlighting critical

anatomical structures or pathologies that may be otherwise challenging to discern [20], enabling surgeons to pinpoint the incision site without direct physical contact. Currently, AR has proven its reliability and efficacy in mapping target regions during surgical interventions. Notably, in a study by Bhatt et al., [21], AR was employed in 222 skew placement experiments during spinal surgeries, achieving an impressive success rate of 98.2%. Furthermore, the introduction of an AR-assisted lumbar puncture guidance system [22] shows promising enhancements in needle navigation accuracy, potentially reducing failure rates in lumbar puncture procedures.

Therefore, this study aims to develop an AR guidance strategy with real-time optical tracking capabilities to support the localization of incision sites during tracheostomy procedures shown in Fig. 1. This work contributes the following:

- Integrating ultrasound information from laryngeal phantom models with varying cortical thicknesses as visual markers to guide the incision site;
- Accomplished precise label of the target region for cricothyroidotomy and tracheostomy, virtual-to-real registration, and effectively integrated it into the AR display;
- Conducted comparative trials utilizing laser-assisted localization accuracy between naked eyes and AR-guided procedures, confirming the reliability of AR-guided incision site localization.

II. METHODOLOGY

A. Acquiring Preoperative Laryngeal Information

To obtain detailed structural insights into the subcutaneous structure of the larynx region and to facilitate precise delineation of the ROI, we employed an ultrasound probe to conduct B-mode scanning of the 3D printed laryngeal model. The depicted throat structures include the thyroid cartilage, cricoid cartilage, and tracheal rings. The thyroid cartilage is located in the upper part of the throat and resembles a shield. Below the thyroid cartilage is the cricoid cartilage, which forms a ring-like shape and is an important component of the throat. The tracheal rings are a series of ring-shaped structures that connect the cricoid cartilage to the trachea located below. Additionally, Fig. 2 shows a spliced view obtained from ultrasound B-mode imaging. Tracheal cavity regions with more distinct interfaces will produce stronger echo signals, appearing brighter in the image. Conversely, if sound waves are absorbed, scattered, or attenuated within the tracheal cartilage regions, the echo signals will be weaker, leading to darker areas in the image. The labeled positions indicated as l_i ($n=1,2,3,4,5,6,7,8$) provide reference points for different locations or structures within the throat. Ultrasound B-scan mode is utilized for length measurements and evaluating the variation in length error and helps in understanding the layered structure of the throat and the relative positions of various structures. By analyzing this data, we can understand the trends and magnitude of length errors at different locations.

Given the impact of the fat layer thickness in the larynx on ultrasound imaging accuracy in clinical settings, we

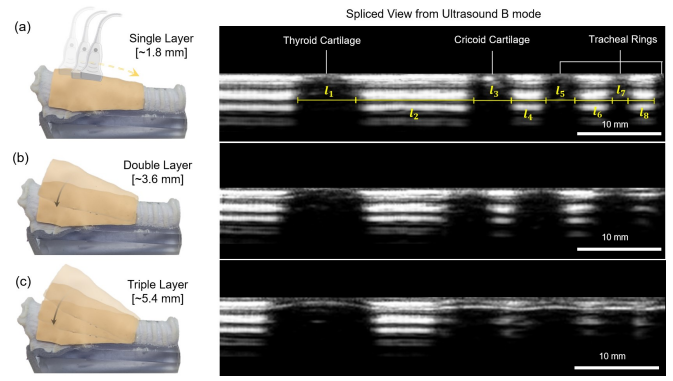


Fig. 2. Ultrasound B-scan imaging view depicting three configurations of the throat phantom: (a) single-layer, (b) double-layer, and (c) triple-layer.

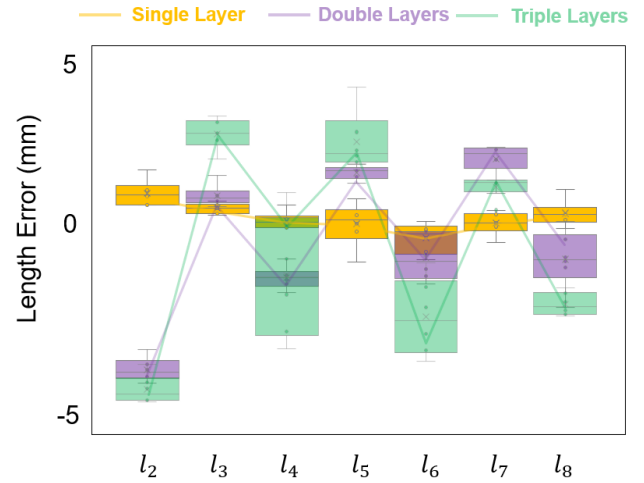


Fig. 3. Length estimation error using ultrasound B-scan mode under the single-layer, double-layer, and triple-layer configurations.

conducted a comparative test involving three cortical single-layer, double-layer, and triple-layer configurations to assess their performance. Fig. 3 shows that the length error refers to the difference between the actual measured value and the theoretical or expected value under the single-layer, double-layer, and triple-layer configurations. In ultrasound-based throat structure detection, minimal error occurs with a single layer of approximately 1.800 mm thickness. The measurement errors in ultrasonic scanning varied within the following ranges: -0.451 mm to 0.584 mm for the single-layer setup, -3.494 mm to 4.632 mm for the double-layer arrangement, and -4.527 mm to 2.325 mm for the triple-layer configuration. It indicates that with an increase in the number of layers and their thickness, the precision of individual components in ultrasound detection diminishes. This is primarily evident through overestimation in raised areas and underestimation in recessed regions relative to actual measurements.

B. System Integration and Calibration

The proposed system mainly involves two steps: labeling the ROI on the laryngeal phantom model based on US

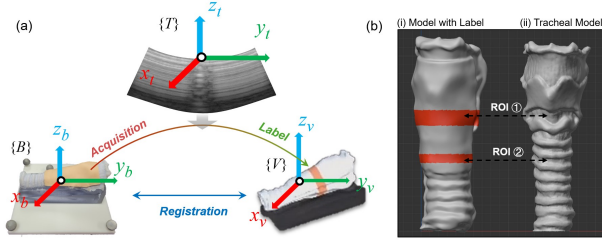


Fig. 4. (a) registration process between the labeled model and the tracheal model; (b) labeled tracheal model based on the US information with two regions of interest corresponding to the cricothyroidotomy and standard tracheostomy.

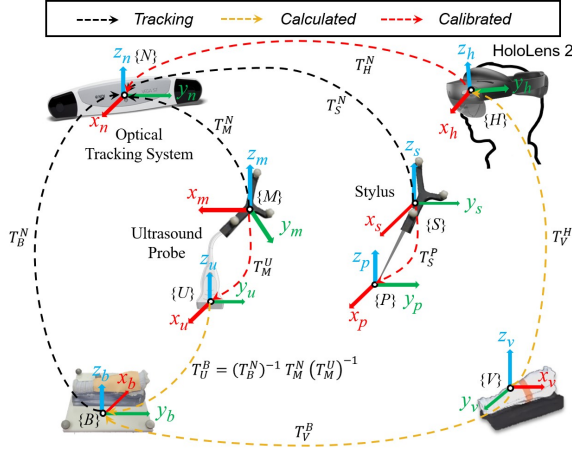


Fig. 5. System coordinate transformation relationship.

information and registering the virtual model on the real phantom for real-time observation. Following the acquisition of laryngeal anatomy information using the US probe with optical markers, we can correlate and label ultrasound information with relative positions between the US probe and the laryngeal phantom. More explicitly, the incision location for the standard tracheostomy site is identified as the gap l_2 between the second and third tracheal rings, while the incision for the cricothyroidotomy site is pinpointed at the gap l_8 between the cricothyroid cartilage and the thyroid cartilage. The labeling process has been completed using the software Cinema 4D, a 3D drawing software developed by Maxon, and the ROI is accentuated based on the measured relative position.

Our system consists of two basic coordinate systems: the optical tracker frame N, and the virtual frame H. The corresponding virtual model V with ROI is rendered in the virtual frame by Unity. To accurately overlay the virtual model on the real model, T_V^H , the pose of the V in the virtual frame H is required. As shown in Fig. 5, the calculation requires two calibrations: registering the real model B in the tracker frame N and calibrating the transformation T_H^N from the tracker frame N to the virtual frame H.

At first, by utilizing the 3D Slicer, the real phantom is registered in the tracker frame N, whose pose is T_B^N . A US probe with three fiducial markers is also tracked by N, whose pose is T_M^N . Based on the T_M^N , the transformation T_M^U between the

Algorithm 1 Virtual-to-real calibration

Input: The position of seven virtual points P_V rendered in the HoloLens 2; Sampling times X for each points.

Output: Transformation matrix T_H^N for the calibration.

```

1: for  $i < 7$  do
2:   for  $j < X$  do
3:      $P_{N_j} = T_P^N$ 
4:   end for
5:   i-th virtual point from frame N:  $P_{N_i} = \frac{1}{X} \sum_{j=1}^X P_{N_j}$ 
6: end for
7: Landmark registration between  $P_V$  and  $P_N$ 
8: return  $T_H^N$ 

```

tip U and the fiducial markers M can be calculated through the pivot calibration, which is implemented by rotating the US probe around its tip. Now the transformation T_U^B between the US probe U and the real phantom B can be calculated as

$$T_U^B = (T_B^N)^{-1} T_M^N (T_M^U)^{-1}. \quad (1)$$

Based on the transformation, an accurate virtual model V with ROI can be created.

The virtual-to-real calibration equals to find the transformation between the tracker N and the virtual frame H. To finish the calibration, a virtual calibration board, which consists of seven points, are used. The position of each virtual point in H is P_V , which can be acquired by the HoloLens 2 once the virtual calibration board is rendered.

Afterwards, a stylus with three fiducial markers is used to find the corresponding position of the virtual points in the tracker frame N. The fiducial markers S are tracked by the optical tracker, whose pose is T_S^N . Based on the T_S^N , the transformation T_S^P between the stylus tip P and the fiducial markers S can also be calculated through the pivot calibration. When the HoloLens 2 is worn, the user can touch the virtual points with the stylus tip, whose pose in the tracker frame is T_P^N . The pose is calculated as

$$T_P^N = T_S^N (T_S^P)^{-1}. \quad (2)$$

To maintain stable tracking results, the stylus will engage with the virtual points X times, with each virtual point's position in frame N represented as P_{N_i} . Employing Algorithm 1, the transformation T_H^N from frame N to H can be ascertained through Singular Value Decomposition (SVD), a conventional method for landmark registration solutions.

In addition, the virtual model V is rendered in the virtual frame H, which is created by Unity3D. In this case, V is in the left-handed coordinate. Then, the negative z-axis in the virtual system is set as the new z-axis to acquire a new pose in the right-handed coordinate system. Finally, a transformation T_V^B to the new frame is performed, which ensures that the coordinate alignment.

The kinematic chain is now established, and the goal transformation T_V^H can be calculated by

$$T_V^H = (T_H^N)^{-1} T_B^N T_V^B. \quad (3)$$

This result will be utilized to finalize the virtual-to-real calibration process.

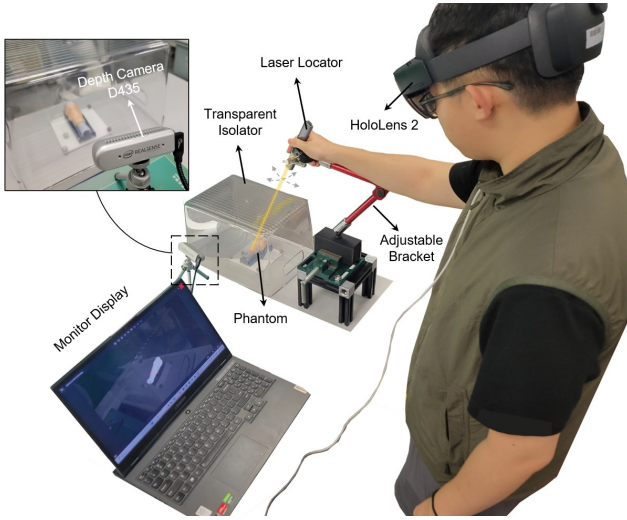


Fig. 6. The experimental setup for laser positioning.

III. EXPERIMENT

A. Laser Positioning Experiment

In laparoscopic surgery, surgical laser locators are often introduced to assist surgeons in efficiently positioning trocar insertions. Inspired by this practice, to validate the effectiveness of incision recommendations in the tracheostomy under AR guidance, we conducted laser localization experiments to compare the precision rate of incision positioning when operating the laser locator under naked-eye conditions versus under AR guidance. Fig. 6 shows the components of the laser positioning experimental setup. The transparent isolator serves the purpose of simulating a surgical isolation chamber. It creates a controlled environment that mimics the conditions of the isolated surgical setting. The surgeon can manipulate the adjustable bracket and hold the surgical laser locator in place through the bracket. The bracket allows for fine-tuning the angle, height, or position of the laser locator to achieve accurate laser targeting. HoloLens 2 as mentioned can provide virtual ROI overlays and anatomy information to the surgeon. In the context of the experimental setup, HoloLens 2 can be used to project virtual surgical guidance, anatomical structures, or real-time data onto the surgeon's field of view. The tracheal phantom is selected using the single-layer configuration, which serves as a substitute for real human tissue during training or experimental procedures. During the laser positioning experiment, the RealSense D435 depth camera is used to record the fall positions of the laser point on the tracheal phantom.

In this experiment, we have expanded our analysis to include the precise localization of two additional critical incision sites: the cricothyroid ligament area for cricothyroidotomy and the specific tracheal tube location for standard tracheostomy, as depicted in Fig. 7(a). Fig. 7(b) provides a detailed visualization of the incision points for cricothyroidotomy and standard tracheostomy as seen through the AR perspectives. Subsequently, Fig. 7(c) and (d) illustrate the laser guidance procedures employed during cricothyroidotomy and standard tracheostomy.

TABLE I
RESULTS OF LASER POSITIONING EXPERIMENTS

Surgical Training Scene	Naked Eyes		AR Guidance	
	TP	FP	TP	FP
Cricothyroidotomy [n=116]	50	7	55	4
Tracheostomy [n=324]	19	143	152	10

B. Positioning Classification Results

In order to further validate the effectiveness of AR guidance, we conducted multiple comparative experiments to enhance the persuasiveness. We conducted a total of 440 laser positioning experiments, considering two types of surgical positioning scenarios: incision location guidance in cricothyroidotomy (n=116) and tracheotomy (n=324)¹. To ensure experimental fairness, the participants in the laser localization experiment were allowed to examine the laryngeal model before securing the transparent isolator, using both AR glasses and the naked eye as control variables. This step aimed to provide testers with sufficient a priori information once the experiment began.

Here, we define cases where the laser point is guided into the target area as true positive (TP) cases, and the ones where the laser point is positioned outside the target area as false positive (FP) cases. The experimental results show that during cricothyroidotomy incision guidance experiments, under naked-eye guidance, there were 50 TP cases and 7 FP cases; under AR guidance, there were 55 TP cases and 4 FP cases. For tracheotomy incision guidance experiments, under naked-eye guidance, there were 19 TP cases and 143 FP cases; under AR guidance, there were 152 TP cases and 10 FP cases. Based on the above information, we proceed to calculate the localization precision (P_i) under naked-eye guidance and AR guidance using the formula:

$$P_i = \frac{TP_i}{TP_i + FP_i}. \quad (4)$$

For cricothyroidotomy, under naked-eye guidance, the localization precision is approximately 0.877, while under AR guidance, it is around 0.932. For tracheotomy, the precision under naked-eye guidance is roughly 0.117, whereas under AR guidance, it is about 0.938. These calculations reveal that in cricothyroidotomy, the precision under AR guidance is close to that under naked eye guidance. The reason can be analyzed as that the target area in cricothyroidotomy may be relatively clear and the target area is large enough to be easily observed and localized by the operator, making the accuracy of naked-eye guidance similar to that of AR guidance. However, in tracheotomy, the precision under AR guidance significantly outperforms that under naked-eye guidance. This underscores the effectiveness of using AR guidance systems in enhancing the precision of surgical incision positioning experiments.

C. Center Positioning Performance

To enhance the validation of the safety of AR guidance, we conducted additional measurements to quantify the distance of the laser dot from the center point of the region following

¹The laser positioning dataset can be accessible through here.

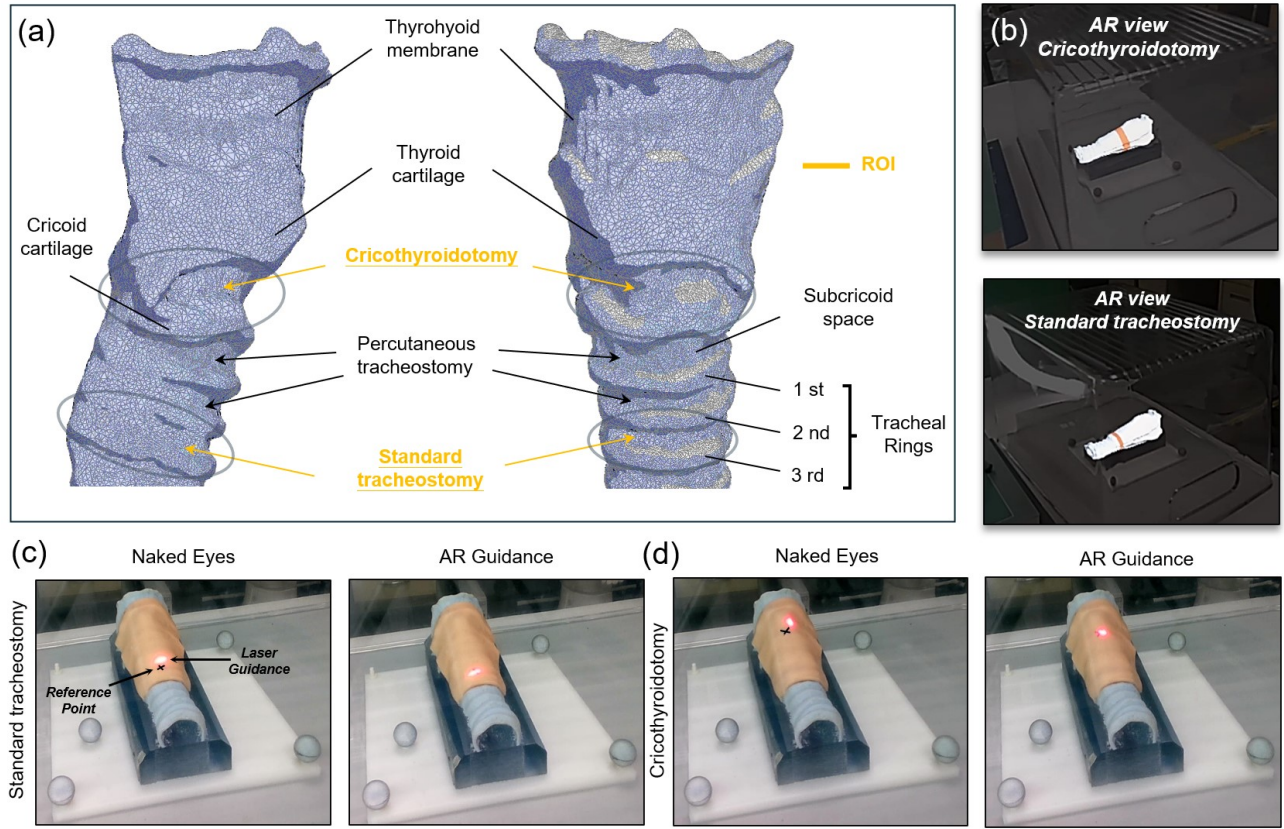


Fig. 7. (a) shows the anatomical structures of larynx regions such as the tracheal rings and the cricoid cartilage. It highlights the location of the cricothyroidotomy and references the thyroid cartilage and thyrohyoid membrane as relevant anatomical landmarks; (b) the diagram includes references to the AR guidance, which highlights the incision location of the cricothyroidotomy and standard tracheostomy; (c) and (d) laser guidance procedure in cricothyroidotomy and standard tracheostomy. Both procedures incorporate laser guidance based on the naked eye and AR guidance for comparative analysis.

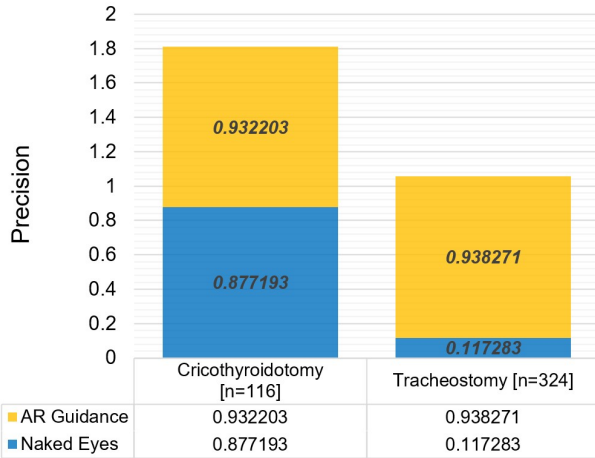


Fig. 8. Laser positioning precision performance of the cricothyroidotomy and tracheostomy scenes under AR guidance and naked eyes.

its impact on the region of interest. The Histogram analysis in Fig. 9 reveals a fairly uniform distribution without significant outliers. As for the cricothyroidotomy scene, Fig. 9 (a) shows that the mean error of naked-eye positioning is 0.291 mm, and the range of the data is 0.671 mm. Fig. 9 (b) shows the

mean error of AR-guided positioning is 0.301 mm; while for the standard tracheostomy scene, Fig. 9 (c), the mean error of naked-eye positioning is 0.264 mm. Fig. 9 (d) shows the mean error of AR-guided positioning is 0.236 mm, with a median error of 0.224 mm and a data range of 0.604 mm. The findings highlight the nuanced effectiveness of AR-guided incision localization across varying surgical scenarios. In cricothyrotomy situations with ample incision space, both naked-eye observation and AR-guided methods demonstrate comparable performance in success rates and centering accuracy. Conversely, in more intricate standard tracheostomy scenarios characterized by limited incision areas, the AR-guided approach notably outperforms naked-eye localization, showcasing superior success rates and enhanced precision in centering the incision point. These results underscore the potential benefits of AR guidance in improving surgical outcomes, particularly in challenging anatomical contexts requiring precise incision localization.

IV. CONCLUSION AND FUTURE WORKS

In this study, we have explored the use of AR technology to assist in tracheostomy insertions. By utilizing a handheld ultrasound probe to acquire preoperative anatomical data from a larynx phantom, marking the ROI, and importing it into the Hololens device, we have achieved visual guid-

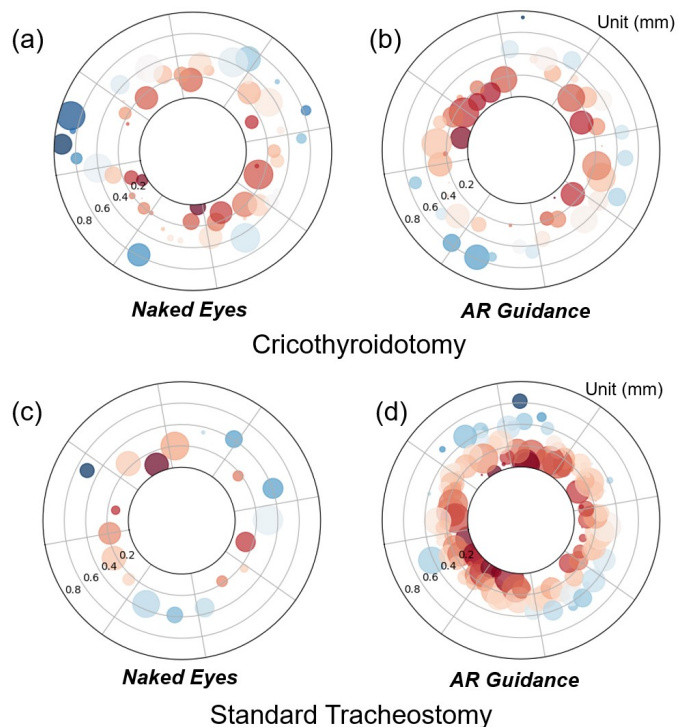


Fig. 9. Central distance error on the polar axis between the laser indication's center point and the target area's center point considering all the TP cases of the cricothyroidotomy and tracheostomy scenes under AR guidance and naked eyes.

ance for precise incision insertion. We have also demonstrated through laser localization comparison experiments that compared with naked-eye guidance, AR guidance enables surgeons to locate the corresponding laryngeal area efficiently, thereby facilitating the progress of robot-assisted tracheostomy. In clinical practice, we have observed that the combination of AR technology with the surgical laser locator can enhance the precision and safety of tracheostomy procedures, ultimately improving patient outcomes. Our future work will incorporate such AR-assisted multimodal information-guided incision positions into the robot's control system to enhance and ground the feasibility of robot-assisted tracheostomy procedures.

REFERENCES

- [1] M. Vargas, Y. Sutherasan, M. Antonelli, I. Brunetti, A. Corcione, J. G. Laffey, C. Putensen, G. Servillo, and P. Pelosi, "Tracheostomy procedures in the intensive care unit: an international survey," *Critical Care*, vol. 19, pp. 1–10, 2015.
- [2] J. D. Cooper, "Surgery of the airway: historic notes," *Journal of Thoracic Disease*, vol. 8, no. Suppl 2, p. S113, 2016.
- [3] B. Herritt, D. Chaudhuri, K. Thavorn, D. Kubelik, and K. Kyeremanteng, "Early vs. late tracheostomy in intensive care settings: Impact on icu and hospital costs," *Journal of critical care*, vol. 44, pp. 285–288, 2018.
- [4] N. H. Cheung and L. M. Napolitano, "Tracheostomy: epidemiology, indications, timing, technique, and outcomes discussion," *Respiratory care*, vol. 59, no. 6, pp. 895–919, 2014.
- [5] N. Siddiqui, C. Arzola, Z. Friedman, L. Guerina, and K. E. You-Ten, "Ultrasound improves cricothyrotomy success in cadavers with poorly defined neck anatomy: a randomized control trial," *Anesthesiology*, vol. 123, no. 5, pp. 1033–1041, 2015.
- [6] H. Flaatten, S. Gjerde, J. Heimdal, and S. Aardal, "The effect of tracheostomy on outcome in intensive care unit patients," *Acta anaesthesiologica scandinavica*, vol. 50, no. 1, pp. 92–98, 2006.
- [7] Y. Zhang, X. Wei, W. Yue, C. Zhu, and F. Ju, "A dual-mode tactile hardness sensor for intraoperative tumor detection and tactile imaging in robot-assisted minimally invasive surgery," *Smart Materials and Structures*, vol. 30, no. 8, p. 085041, 2021.
- [8] H. C. Grillo, *Surgery of the Trachea and Bronchi*. PMPH USA, 2004.
- [9] J. Y. Chew and R. W. Cantrell, "Tracheostomy: complications and their management," *Archives of Otolaryngology*, vol. 96, no. 6, pp. 538–545, 1972.
- [10] T. Li, J. Guo, H. Zheng, S. Wang, L. Qiu, and H. Ren, "Fault-tolerant six-axis fbg force/moment sensing for robotic interventions," *IEEE/ASME Transactions on Mechatronics*, 2023.
- [11] R. Tang, S. Yao, L. Bai, H. Yan, M. Q.-H. Meng, and H. Ren, "Data-driven 3d tactile cues with intermediate soft interfaces towards training needle insertions," *IEEE Sensors Journal*, 2024.
- [12] W. Yue, F. Ju, Y. Zhang, Y. Yun, T. Li, Z. T. H. Tse, and H. Ren, "Dynamic piezoelectric tactile sensor for tissue hardness measurement using symmetrical flexure hinges and anisotropic vibration modes," *IEEE Sensors Journal*, vol. 21, no. 16, pp. 17 712–17 722, 2021.
- [13] F. Ju, Y. Hong, D. Bai, Z. Yin, C. Zhu, and W. Yue, "A laminated continuum robot with gripping force-sensing forceps for robot-assisted minimally invasive surgeries," *IEEE Sensors Journal*, vol. 23, no. 1, pp. 766–774, 2022.
- [14] Y. Tang, L. Li, Z. Lu, A. Haron, B. V. Adorno, B. McGrath, and A. Weightman, "Design requirements of robotic systems for assisting percutaneous tracheostomy: a scoping review and development framework," *IEEE Transactions on Medical Robotics and Bionics*, 2023.
- [15] X. Xiao, H. Poon, C. M. Lim, M. Q.-H. Meng, and H. Ren, "Pilot study of trans-oral robotic-assisted needle direct tracheostomy puncture in patients requiring prolonged mechanical ventilation," *Frontiers in Robotics and AI*, vol. 7, p. 575445, 2020.
- [16] M. Botyrius, Q. Liu, C. M. Lim, and H. Ren, "Design conceptualization of a flexible robotic drill system for minimally invasive tracheostomy," in *2018 IEEE International Conference on Real-time Computing and Robotics (RCAR)*. IEEE, 2018, pp. 584–588.
- [17] W. Yue, F. Bai, J. Liu, F. Ju, M. Q.-H. Meng, C. M. Lim, and H. Ren, "Rasec: Rescaling acquisition strategy with energy constraints under fusion kernel for active incision recommendation in tracheostomy," *IEEE Transactions on Automation Science and Engineering*, 2024.
- [18] H. Gao, X. Xiao, L. Qiu, M. Q.-H. Meng, N. K. K. King, and H. Ren, "Remote-center-of-motion recommendation toward brain needle intervention using deep reinforcement learning," in *2021 IEEE International Conference on Robotics and Automation (ICRA)*. IEEE, 2021, pp. 8295–8301.
- [19] N. Shihora, R. Yasin, R. Walsh, and N. Simaan, "Feasibility of remote landmark identification for cricothyrotomy using robotic palpation," in *2021 IEEE/RSJ International Conference on Intelligent Robots and Systems (IROS)*. IEEE, 2021, pp. 1808–1814.
- [20] L. Qian, J. Y. Wu, S. P. DiMaio, N. Navab, and P. Kazanzides, "A review of augmented reality in robotic-assisted surgery," *IEEE Transactions on Medical Robotics and Bionics*, vol. 2, no. 1, pp. 1–16, 2019.
- [21] F. R. Bhatt, L. D. Orosz, A. Tewari, D. Boyd, R. Roy, C. R. Good, T. C. Schuler, C. M. Haines, and E. Jazini, "Augmented reality-assisted spine surgery: an early experience demonstrating safety and accuracy with 218 screws," *Global Spine Journal*, vol. 13, no. 7, pp. 2047–2052, 2023.
- [22] B. Jiang, L. Wang, K. Xu, M. Hossbach, A. Demir, P. Rajan, R. H. Taylor, A. Moghekar, P. Foroughi, P. Kazanzides *et al.*, "Wearable mechatronic ultrasound-integrated ar navigation system for lumbar puncture guidance," *IEEE Transactions on Medical Robotics and Bionics*, 2023.